Exchange-biased nanocomposite ferromagnetic insulator

Ji Zhang [1], Jingtian Zhou,[2] Zhen-Lin Luo,[2,*] Y. B. Chen,[3] Jian Zhou [1], Weiwei Lin [4], Ming-Hui Lu,[1] Shan-Tao Zhang [1,†]
Chen Gao,[5] Di Wu,[1] and Yan-Feng Chen[1]

[1]*National Laboratory of Solid State Microstructures, Department of Materials Science and Engineering, College of Engineering and Applied Science and Jiangsu Key Laboratory of Artificial Functional Materials and Collaborative Innovation Center of Advanced Microstructures, Nanjing University, Nanjing 210093, China*
[2]*National Synchrotron Radiation Laboratory and Chinese Academy of Sciences Key Laboratory of Materials for Energy Conversion, University of Science and Technology of China, Hefei, Anhui 230026, China*
[3]*National Laboratory of Solid State Microstructures and School of Physics and Collaborative Innovation Center of Advanced Microstructures, Nanjing University, Nanjing 210093, China*
[4]*Department of Physics and Astronomy, Johns Hopkins University, Baltimore, Maryland 21218, USA*
[5]*Beijing Advanced Sciences and Innovation Center of Chinese Academy of Sciences, Beijing 101407, China*

Magnetic insulating and exchange bias (EB) are two basic magnetic states with actual and potential applications in spintronic and magnonic devices. However, ferromagnetic insulators (FMIs) are rare, and it is even more challenging to obtain a FMI with large EB. In this paper, high performance of FMIs and EB in $LaMnO_3$:NiO nanocomposite epitaxial thin films is reported. The antiferromagnetic NiO nanoparticles, randomly embedded in a ferromagnetic $LaMnO_3$ matrix, enhance the robustness of the insulating state and result in an EB field as large as 1100 Oe. The simultaneously enhanced resistivity and EB are attributed to localized oxygen vacancy, preserved strain state, and increased ferromagnetic-antiferromagnetic interface ratio. This paper provides not only a material candidate for spintronics but also a referential strategy to design artificial materials with multifunctionality.

I. INTRODUCTION

Insulating magnets are highly desired materials for magnetoelectric devices, for ultrafast spin-optical recording, and recently for efficient generation and transmission of magnonic spin current free of electronic charge flow, and thus with minimal Joule heating and low power dissipation [1–4]. Among insulating magnets, ferromagnetic insulators (FMIs) allow emergence of some prominent phenomena with novel physics and open new possibilities for spin-orbit interaction related spintronic devices [5–9]. Perovskite oxide FMIs, which can be ideally integrated with many single-crystal substrates, are relatively rare [7]. Some bulk antiferromagnetic insulating perovskite oxides show ferromagnetic behavior in strained thin-film form. Among them, $3d$ transition-metal oxide $LaMnO_3$ (LMO) thin film is of particular interest partly due to its relatively high Curie temperature ($T_c \approx 100$ K) [9,10]. However, insulating behavior of LMO thin films is not robust and can be easily suppressed or even destroyed by strain relaxation and/or chemical defects like oxygen vacancy (V_O''), both of which are inevitable in thin films and can change the local symmetry and the cation's valance [11–17].

On the other hand, exchange coupling between ferromagnet and antiferromagnet (AF), leading to exchange bias (EB) effect, is mostly studied in ferromagnetic or ferrimagnetic metals, but few works have been explored in FMIs [18–23]. In recent years, EB effect has been observed in LMO-based superlattices [14,22–25], but the EB field is far lower than that in conventional magnetic metals [19,21,26,27] because of the lack of direct exchange coupling and the itinerant electron mediated coupling. Accordingly, both FMI and EB behaviors in LMO-like thin films need further improvements. Moreover, besides viewpoints of fundamental physics, the coexistence of FMIs and EB can provide an additional freedom for novel device design. For example, exchange-biased FMIs can provide a biased magnetic field in the electronic device without any charge-carrier contribution. More importantly, in analogy to the well-used exchange-biased spin valve in the read head of hard disk and magnetic random access memory, the exchange-biased FMI can be used in a magnon valve for novel magnon-based devices. Intuitively, coexistence of FMIs and EB is feasible since, similarly to FMIs, EB is sensitive to strain relaxation and defects like V_O'' [22–24].

However, conventional heterostructure with a two-dimensional (2D) interface is not an appropriate strategy for realizing integrated robust FMIs and EB because of the following:

(1) The 2D ferromagnetic/antiferromagnetic interface usually decreases resistivity, thus suppressing insulating behavior, since it cannot prevent the long-distance migration of charges or charged defects like V_O' along the interfacial 2D plane [22–25,28,29].

(2) The strain arising from substrate-film lattice mismatch tends to relax along the normal direction of the

*Corresponding author: zlluo@ustc.edu.cn
†Corresponding author: stzhang@nju.edu.cn

heterostructure, which induces thickness-dependent macroscopic properties like ferromagnetism or insulating behavior. That is, some unusual properties can only be achieved in ultrathin films [30–32].

Therefore, an alternative interface to prevent the migration of charges and defects and to sustain the strain in relatively thick films is preferred. In our opinion, the so-called 0–3-type LMO:NiO nanocomposite thin films, where antiferromagnetic insulating NiO nanoparticles are embedded in a three-dimensional (3D) FMI LMO matrix, offer a promising strategy to realize robust FMIs and EB simultaneously because of the following considerations.

(1) Zero-dimensional (0D) NiO nanoparticles can act as charge reservoirs to trap and localize the transferred charge or defects like V_O'' from the 3D LMO matrix due to the variable chemical valence of Ni cations [23,33], as well as the higher Pauling electronegativity of Ni (1.91) compared with Mn (1.55).

(2) NiO nanoparticles distribute randomly but homogeneously in macroscopic scale, thus the strained state of LMO can be sustained or even strengthened along all three directions [34–36].

(3) The high specific surface of NiO nanoparticles ensures a large total interfacial area between LMO and NiO, which is helpful to enhance the above two desired effects.

Here we report the coexistence of robust FMIs and large EB in 0–3-type $(1 - x)$LMO : xNiO nanocomposite epitaxial thin films on (001)-SrTiO₃ (STO) substrates, where x represents the mole ratio of NiO. The nanocomposite structure is utilized to increase the FM-AF interface ratio to the bulk, and thus the EB can be enhanced by more than one order of magnitude compared with that in the bilayer. With the optimal composition, the resistivity is about 15 times larger than that of the pure LMO films within the whole measuring temperature range, and the EB field is as large as 1100 Oe.

II. EXPERIMENTAL METHODS

$(1 - x)$LMO : xNiO ($x = 0-0.6$ with intervals of 0.1) ceramics used as targets for film deposition were prepared by conventional solid-state reaction. Thin films were deposited on (001)- STO substrates by pulsed laser deposition using a 248-nm KrF excimer laser. The chamber was evacuated to a base pressure of 10^{-8} mbar before deposition. During each deposition, the substrate temperature was $800\,°C$, the laser repetition rate was 2 Hz, the laser energy density was $1.2\,J/cm^2$, and the flowing oxygen pressure was 0.05 mbar. After deposition, the films were *in situ* annealed in the chamber for 10 min, cooled to $400\,°C$ with the rate of $-15\,°C/min$, then cooled to room temperature naturally.

It should be noted that to obtain high-quality LMO:NiO nanocomposite thin films two factors should be considered. One is the NiO content. Too high NiO content leads to aggregation of nanosized NiO into large particles. The other is the sample preparation process. Especially, the sintering temperature and sintering time during ceramic target preparation, and the deposition temperature and deposition oxygen pressure during thin-film preparation, are the key factors determining the distribution and size of NiO particles. Briefly, the LMO powders were prepared by solid-state reaction.

The stoichiometric La₂O₃ and MnO₂ powders were mixed, ball milled in ethonal for 24 h, and sintered at $1200\,°C$ for 20 h with increasing temperature of $5\,°C/min$ from room temperature. Then the LMO and NiO powders were weighted according to $(1 - x)$LMO : xNiO ($x = 0-0.6$); the mixtures were ball milled for 1 h, dried, and pressed into 24-mm diameter and about 2-mm thickness. The disks were sintered at $1100-1200\,°C$ depending on composition for 1 h with a relatively rapid increasing temperature rate of $10\,°C/min$. Powder x-ray-diffraction (XRD, Bruker D8) patterns of the ceramics are plotted in the Supplemental Material Fig. S1 [37]. Two important issues should be addressed.

(1) LMO ceramic is single phase whereas composite ceramics with $x > 0$ show two sets of diffraction patterns arising from LMO and NiO, as indicated by symbols. Some weak diffraction peaks from third phases can be seen.

(2) The crystal structure of LMO changes from the orthorhombic structure of $x = 0$, 0.1 [38,39] to unexpected tetragonal-like [40]. We believe such phase transition should be attributed to NiO-induced internal strain. Though Ni might enter into the LMO lattice to induce structure distortion, such diffusion and structural distortion should be limited and localized around the LMO/NiO interface, which means the cation's diffusion should not be the determinative effect for the observed phase transition.

The crystal structure of the films was investigated by high-resolution x-ray diffraction (Bruker D8 Discover diffractometer) and synchrotron radiation XRD at beamline 14B of the Shanghai Synchrotron Radiation Facility. The surface morphology and microstructure of the films were recorded by atomic force microscopy (AFM, Cypher) and transmission electron microscopy (TEM, FEI Tecnai F20). The cross-section sample for TEM was prepared by ion milling with 3.2–4.5-keV Ar⁺ ions for a few hours after mechanical thinning. The transport data were collected by a physical property measurement system (PPMS-9, Quantum Design), and the magnetic property was measured by a superconducting quantum interference device (MPMS-3, Quantum Design). The valence state of Mn and Ni ions was characterized by synchrotron radiation x-ray-absorption spectroscopy (XAS) at beamline 12B-a of the National Synchrotron Radiation Laboratory.

III. RESULTS AND DISCUSSION

All thin films show an extremely flat surface, typical surface AFM image, and cross-sectional TEM image of the $x = 0.5$ thin film, shown in Figs. 1(a) and 1(b). The root-mean-square roughness is 131 pm and average thickness is 35 nm. In addition, Fig. 1(b) indicates the desired 0–3 composite microstructure since the random spots with sharp contrast suggest the mixture of NiO and LMO. A high-resolution TEM image [Fig. 1(c)] further proves that isolated 0D NiO nanoparticles with average size of about 2 nm, as typically symbolized by arrows, are randomly embedded in a continuous 3D LMO matrix. The selected area electron diffraction [Fig. 1(d)] confirms that both NiO and LMO are crystallized, and they do form a composite rather than doping. The theoretical volume fraction of LMO to NiO in these nanocomposite films is calculated to be 3.46:1 by considering the density of LMO ($6.37\,g\,cm^{-3}$) and NiO
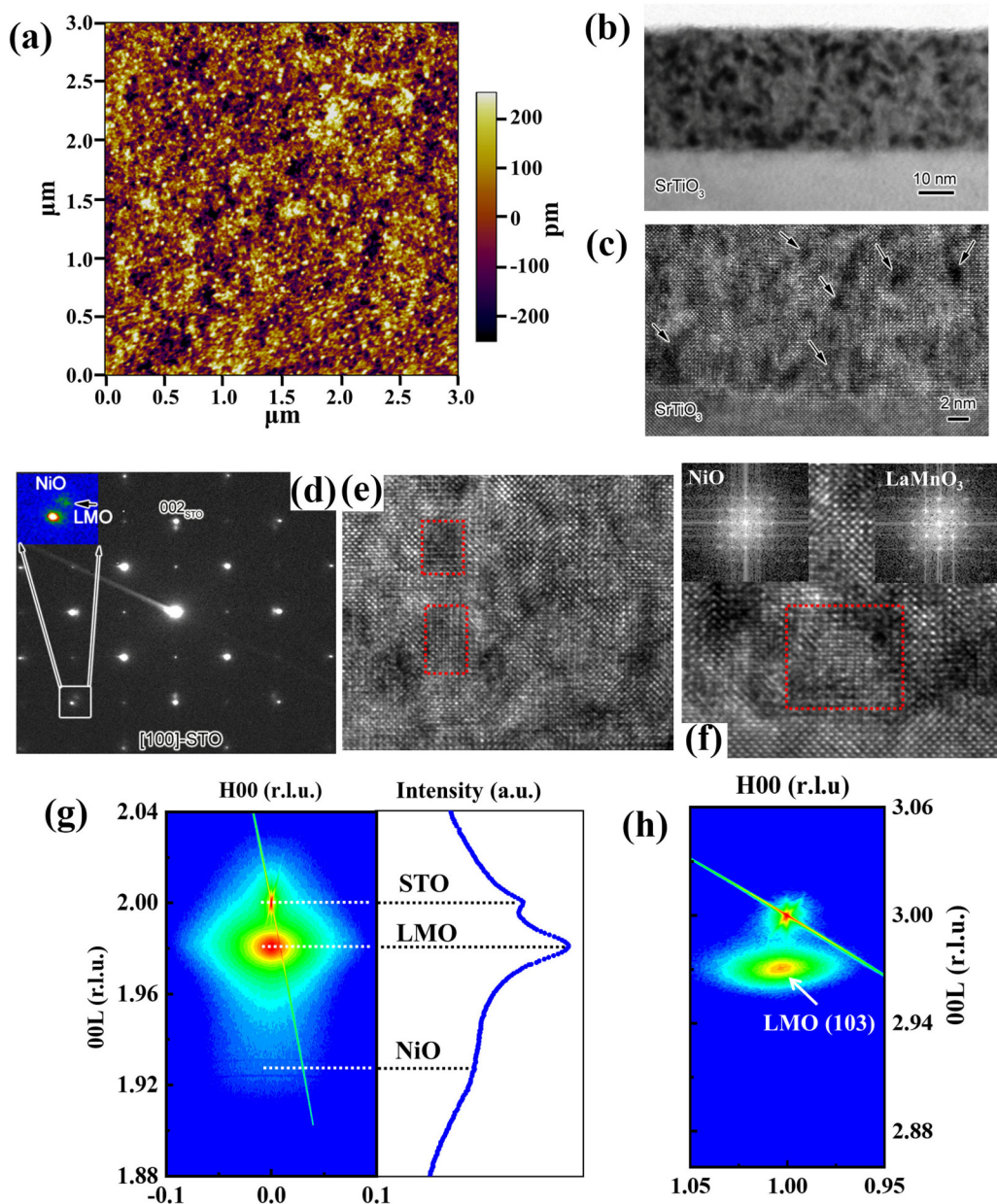
FIG. 1. Structure characterization of the $(1-x)$LMO : xNiO films. (a) The typical AFM image of $x = 0.5$ films shows the extremely flat surface. (b, c) TEM images of $x = 0.5$ films reveal 0–3-type composite structure with nanosized NiO particles; the average film thickness is 35 nm. (d) Selected area electron diffraction (SAED) confirms the epitaxial growth of $x = 0.5$ films. (e, f) Two local high-resolution TEM images near the LMO/NiO interface; the insets of Fig. 1(f) show the fast Fourier-transformation images taken from NiO and LMO. (g, h) Reciprocal space maps around (002) and (103) Bragg spots reaffirm the epitaxial growth and strained state of LMO and NiO in $x = 0.5$ nanocomposite films.

$(6.81 \, \mathrm{g \, cm^{-3}})$. It should be emphasized that in macroscopic scale the NiO particles are nearly homogeneously distributed. Therefore, both LMO and NiO can preserve the strain state throughout the nanocomposite films, though the accurate strain value changes across different NiO contents to some extent.

To further investigate the LMO/NiO interfaces, two local high-resolution TEM images taken far away from the substrate and near the substrate are shown in Figs. 1(e) and 1(f). One can see that NiO particles have epitaxial orientation with respect to the LMO matrix, rather than a textured

structure. Two local fast Fourier-transformation images taken from NiO and LMO are shown in the insets of Fig. 1(f), which also verify the epitaxial relationship between NiO and LMO. Moreover, one can see that the contrast at the boundary between NiO and LMO is quite blurred (highlighted by a red rectangle), and there are misfit dislocations or vacancies nearby. Actually, using the fast Fourier-transformation method, we can see that there are dislocations lying around the boundary between NiO and the LMO matrix. In the field of perovskite thin films, the dislocations are usually composed of the oxygen vacancies in principle [41]. Therefore, it is

reasonable to expect there are oxygen defects accumulated around the interface between NiO and LMO.

Figures 1(g) and 1(h) depict the reciprocal space maps (RSMs) of the $x = 0.5$ films; the appearance of diffraction peaks of LMO and STO confirms the epitaxial growth of LMO. The corresponding lattice parameters of tetragonal-like LMO can be calculated as $a = 3.892$ Å and $c = 3.944$ Å, and that of cubic NiO can be calculated as $a_c = 4.015$ Å. It is noticed that the lattice parameters of LMO in LMO/STO are $a = 3.904$ Å and $c = 3.910$ Å, as calculated from the RSMs in Supplemental Material Fig. S2 [37]. By further comparing with the lattice parameters of bulk LMO ($a_p = 3.990$ Å and $c_p = 3.846$ Å) and NiO ($a_c = 4.177$ Å), we can find that both LMO and NiO in the $x = 0.5$ nanocomposite films are under a strain state, which is in line with our expectation of 0–3-type composite. To further confirm the strain state, θ-2θ XRD scans of the thin films with $x = 0-0.5$ are plotted in Supplemental Material Fig. S3(a) [37]. These patterns show that the LMO are strained and highly textured, consistent with Supplemental Material Fig. S2 [37]. With the increasing NiO content, the (002) diffraction peak of LMO becomes visible to the left of the (002)-STO peak and shifts to a lower angle, as partly enlarged in Supplemental Material Fig. S3(b) [37], which might be attributed to the stretching of the c axis of LMO with the applied out-of-plane tensile stress from NiO. Moreover, the different calculated lattice parameters of LMO in LMO/STO and 0.5LMO:0.5NiO/STO indicate that the strain state of LMO should change across the different NiO compositions to some extent, which is reasonable since the strain state is partly related with the lattice mismatch between LMO and NiO.

The in-plane M-H loops of $x = 0-0.6$ thin films and NiO films were measured at 2 K after field cooling (FC) from 300 K. Typical loops of $x = 0$ and 0.3–0.5 films with $+1$-T field cooling are plotted in Fig. 2(a) while those of $x = 0.6$ films with ± 1-T field cooling and NiO films without field cooling are plotted in Supplemental Material Figs. S4(a) and S4(b) [37], respectively. All $(1 - x)$LMO : xNiO films have well-saturated M-H loops, indicating their macroscopic ferromagnetic nature. The NiO films grown on the STO substrate show weak magnetic hysteresis behavior at $T = 2$ K; however, the magnetization is only 10 emu/cm³, about 20 times smaller than that of $(1 - x)$LMO : xNiO films. The ferromagnetic ordering of individual dislocations in antiferromagnetic NiO may originate from the local nonstoichiometry of the dislocation cores and oxygen vacancies in filaments, leading to the reduction of oxygen-mediated antiferromagnetic coupling [42,43]. The strain in the NiO films on STO substrate and charge transfer at the NiO/STO interface may also contribute to the observed weak ferromagnetism. Note that the NiO nanoparticle structure in the $(1 - x)$LMO : xNiO composite films is very different than that in NiO films on the STO, thus the weak ferromagnetism in the NiO films is not relevant to the ferromagnetism in the $(1 - x)$LMO : xNiO films.

In general, when the ferromagnetic/antiferromagnetic LMO/NiO interface is constructed, EB effect can be observed due to the interfacial interaction if the sample is field cooled down to $T < T_N$ due to the pinned spin [19,21]. In our cases, the 0D antiferroelectric NiO nanoparticles are randomly embedded in the 3D ferromagnetic LMO matrix. Due to the high specific surface of nanoparticles, the effective interface is increased and randomly distributed, thus large and isotropic EB effect can be achieved, as discussed in detail in what follows. The symmetric M-H loops of the $(1 - x)$LMO : xNiO films with $x = 0-0.2$ imply no EB effect, while the shifted M-H loops of the films with $x > 0.2$ indicate EB effect. Both the EB field $H_{EB} = (H_1 + H_2)/2$ and coercive field $H_C = (|H_1| + |H_2|)/2$, where H_1 and H_2 are the magnetic fields corresponding to zero magnetization, increase with x from 0 to 0.5 and then decrease, as illustrated in Figs. 2(a) and 2(b). The first increase of H_{EB} with x is reasonable since EB is due to interfacial exchange coupling; H_{EB} increases with the decrease of the magnetization and the thickness of the ferromagnet and with the increase of the antiferromagnetic thickness. The locally enhanced strain due to NiO inclusions, especially in $x = 0.4$ and 0.5 nanocomposite films as evidenced by the XRD shown in Fig. 1 and Supplemental Material Figs. S2 and S3 [37], should also be positive to increase H_{EB} [22–24]. It is worth emphasizing that the $x = 0.5$ nanocomposite films have the largest H_{EB} of -1100 Oe. Such a H_{EB} value is one order of magnitude larger than that in LMO-based layered heterostructures, about 25 times larger than that of LMO/NiO bilayer films [14,22–25]. This is due to the increase of the FM/AF interface ratio to the bulk in the nanocomposite structure. Moreover, strong interfacial exchange interaction leads to increased H_c at the same time. The further decreased H_{EB} and H_c of $x = 0.6$ should be attributed to the fact that, in these composite films, the NiO particles tend to aggregate, thus the total effective interfacial interaction between NiO and LMO is suppressed. Therefore, the following discussion will focus on the $(1 - x)$LMO : xNiO films with $x \leqslant 0.5$. Additionally, the composition-dependent in-plane M-H loops measured with -1-T field cooling and the corresponding H_{EB} are plotted in Supplemental Material Figs. S5(a) and S5(b) [37], and both are consistent with Figs. 2(a) and 2(b).

From Fig. 2(a), it is also found that saturation magnetization M_s decreases with increasing x from 0 to 0.5. The measured M_s values of the $x = 0$ and 0.5 films are 464 emu/cm³ (2.97 μ_B/Mn) and 185 emu/cm³ (1.19 μ_B/Mn, if neglecting contribution from NiO), respectively. Even considering the volume fraction of 3.46:1, the M_s value of the $x = 0.5$ nanocomposite films is only 246 emu/cm³ (1.58 μ_B/Mn), lower than that of the $x = 0$ (LMO) films. This observation implies two important facts: First, since the V_O''-induced electron usually lowers Mn³⁺ ($t_{2g}^3 e_g^1$) to Mn²⁺ ($t_{2g}^3 e_g^2$) and thus enhances the M_s value due to the ferromagnetic interaction of Mn²⁺-O-Mn³⁺ [14,44], this suppressed M_s value excludes the coexistence of Mn²⁺ in the $x = 0.5$ nanocomposite thin films. In other words, the V_O''-induced electron should be transferred away from the LMO matrix, or the V_O'' is captured and localized by NiO nanoparticles. Second, the Mn⁴⁺ (t_{2g}^3) cation is formed since, in theory, Mn⁴⁺-O-Mn³⁺ has a lower M_s value than Mn³⁺-O-Mn³⁺, which implies that the outside electron of some Mn³⁺ can also be transferred to NiO.

The in-plane M-H loops of $x = 0.3$, 0.4, and 0.5 nanocomposite films were measured at various temperatures (2–20 K) after field cooling from 300 K. Typical results of the $x = 0.5$ films measured at 2, 10, and 20 K with $+1$-T field cooling are shown in Fig. 2(c). One can find that H_{EB} and H_c decrease with increasing temperature, and the H_{EB} value of $x = 0.5$
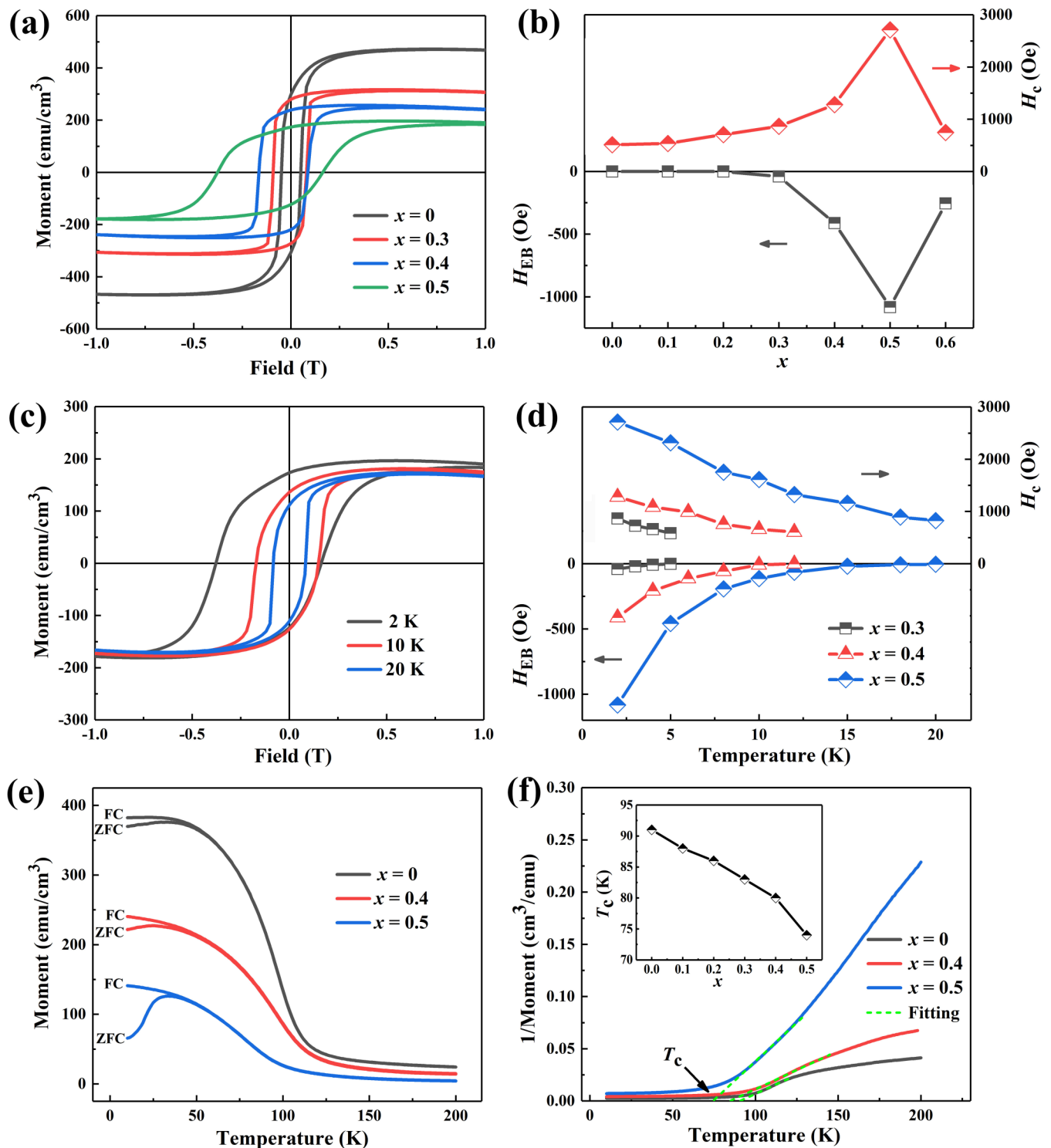
FIG. 2. Magnetic properties of the $(1-x)$LMO : xNiO films. (a) Composition dependent M-H loops measured at 2 K with $+1$-T field cooling. The films with $x > 0.2$ show obvious EB effect. (b) The corresponding composition-dependent H_{EB} and H_c at 2 K. (c) Temperature-dependent M-H loops of $x = 0.5$ nanocomposite films. (d) Temperature-dependent H_{EB} and H_c of $x = 0.3$, 0.4, and 0.5 nanocomposite films. Clearly, there is lower NiO content (x value) and lower blocking temperature. (e, f) Typical FC and ZFC M-T curves (e) and the corresponding $1/M - T$ curves (f) of $x = 0$, 0.4, and 0.5 films. The Curie temperature decreases slightly with increasing x value, as plotted in the inset of Fig. 2(f).

nanocomposite films tends to be zero around 20 K, which refers to the blocking temperature [22–25]. The blocking temperature increases with x, as plotted in Fig. 2(d). It is noted that blocking temperature is much lower than the Néel

temperature of bulk NiO, which is attributed to the finite-size effects of antiferromagnetic NiO nanoparticles [45]. The result measured with -1-T field cooling is quite similar, as illustrated in Supplemental Material Figs. S5(c) and S5(d) [37].
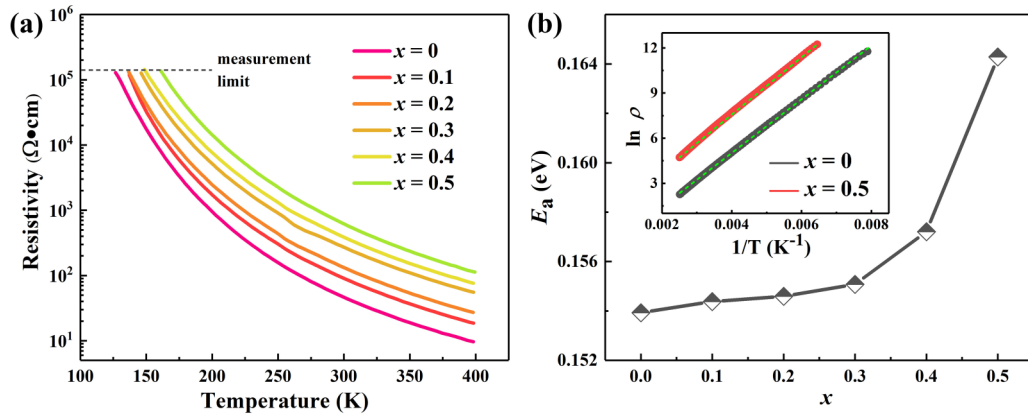
FIG. 3. Resistivity vs temperature of the $(1-x)$LMO : xNiO films. (a) Composition-dependent ρ-T curves of all films show insulating behavior in the whole measuring temperature range. (b) The fitted energy barrier E_a of all films by the Arrhenius formula; the linearly dependent $\ln\rho - 1/T$ curves of typical results of $x = 0$ and 0.5 shown in the inset affirm the thermally activated conduction mechanism.

The out-of-plane *M-H* loops measured at various temperatures with ±1-T field cooling, and the temperature-dependent H_{EB} and H_c of the $x = 0.5$ nanocomposite films, are illustrated in Supplemental Material Fig. S6 [37], which reveals nearly isotropic ferromagnetic nature and EB effect of the nanocomposite thin films since there is no significant difference between the in-plane and out-of-plane results.

Figure 2(e) illustrates the field cooling (0.1 T) and zero-field cooling (ZFC) *M-T* curves of the $x = 0$, 0.4, and 0.5 films. For all films, the magnetization increases smoothly from 200 to 100 K, then increases abruptly and tends to saturate with further decreasing temperature in the FC curve, indicating the paramagnetic-ferromagnetic transition. By plotting the $1/M - T$ curves [Fig. 2(f)], the ferromagnetic T_c is estimated to be about 91 K for the $x = 0$ films, consistent with previous reports [9,10,44]. However, the T_c decreases to 80 and 76 K for the $x = 0.4$ and 0.5 nanocomposite films, respectively. Detailed composition-dependent T_c are shown in the inset of Fig. 2(f). The lowered T_c of nanocomposite films may be due to the enhanced strain.

Figure 3(a) comparatively plots the resistivity vs temperature (ρ-T) of the $x = 0-0.5$ films. For all films, the resistivity increases sharply with decreasing temperature, indicating the insulating behavior. The resistivity increases monotonously with NiO content. For example, at 150 K, the resistivity of the $x = 0$ films is $1.4 \times 10^4 \, \Omega \, \mathrm{cm}$, comparable with or even higher than other reports on perovskite oxide FMI films [6,44,46], while that of the $x = 0.5$ nanocomposite films increases by more than a factor of 10. This observation proves that NiO nanoparticles can significantly enhance the resistivity. The reason for such enhancement should be attributed to charge trapping and localizing ability of NiO, as will be discussed in the following. By fitting the ρ-T curves with the Arrhenius formula of $\rho(T) = \rho_0 \exp(E_a/k_B T)$, where ρ_0 is the preexponential factor, E_a is the activation energy, k_B is the Boltzmann constant, and T is the absolute temperature, one can find the concisely exponential dependence of resistivity on temperature in the whole range. Typical fitting results of the $x = 0$ and 0.5 nanocomposite films are plotted in the inset of Fig. 3(b), which clearly identifies that the conduction is
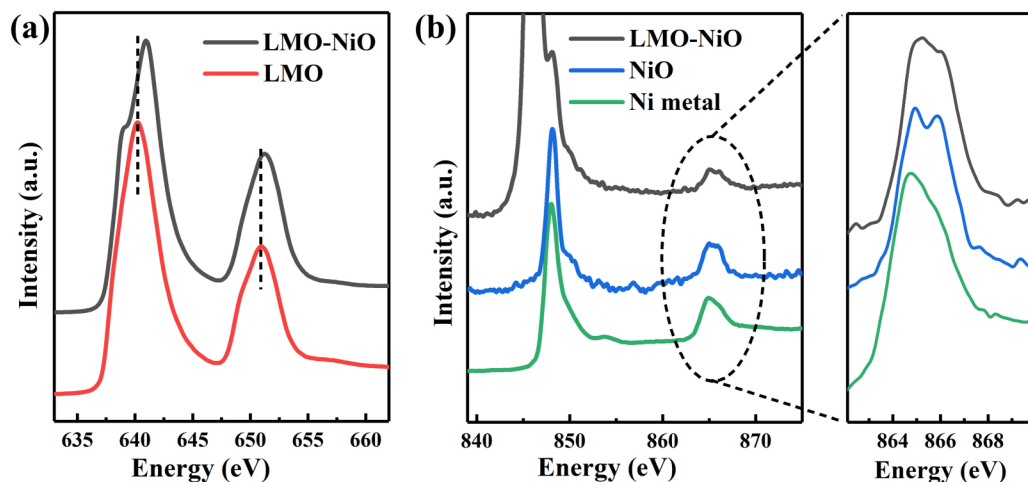

FIG. 4. X-ray-absorption spectrum (XAS) of the LMO films and the $(1-x)$LMO : xNiO films. (a) Mn *L*-edge XAS spectrum measured on the LMO films and the $x = 0.5$ nanocomposite films. (b) Ni *L*-edge XAS spectrum measured on $x = 0.5$ nanocomposite films, NiO films, and Ni metal for comparison. Based on the XAS spectrum, it is concluded that electrons transfer from Mn ions to Ni ions.

thermally activated over an energy barrier with the E_a of 0.154 and 0.164 eV for the $x = 0$ and 0.5 films [47], respectively. Interestingly, the E_a value increases monotonously with x [Fig. 3(b)], which could be attributed to the fact that the increasing strain in the composite films, as indicated by Fig. 1 and Supplemental Material Fig. S2 [37], enhances the energy barrier.

To further understand the coexistence of robust FMIs and EB in LMO:NiO nanocomposite films, Mn L-edge and Ni L-edge XAS spectra were comparatively measured on LMO/STO, 0.5LMO:0.5NiO/STO, NiO/STO heterostructures, and Ni metal, and the results are plotted in Fig. 4. Compared with that of LMO films [down red line in Fig. 4(a)], the Mn L_3 and L_2 peaks of the $x = 0.5$ nanocomposite films [upper gray line in Fig. 4(a)] shift toward the higher-energy side, which proves the presence of Mn^{4+} and absence of Mn^{2+} [14,48,49]. The absence of Mn^{2+} indicates that oxygen vacancy should be trapped and localized around NiO [14,44]. The Ni L_2 peak of the $x = 0.5$ nanocomposite films [upper gray lines in Figs. 4(b) and 4(c)] changes the spectrum shape without obvious peak shift when compared with that of NiO films [middle blue lines in Figs. 4(b) and 4(c)]. However, the Ni L_2 peak of $x = 0.5$ nanocomposite films and NiO films shifts toward high energy and changes the shape when compared with that of Ni metal [down green line in Figs. 4(b) and 4(c)]. Therefore, the Ni L_2 peak indicates that most Ni cations in nanocomposite films keep the $+2$ valence, which means that not all the charge stemming from the Mn cation can be transferred to the Ni cation, which is reasonable since such charge transfer can only occur around LMO/NiO interfaces. In our opinion, some of the charges stemming from Mn cations are trapped at the localized oxygen vacancies near LMO/NiO interfaces, which are confirmed to exist by TEM shown in

Fig. 1(f). Please note that charge transfer from Mn to Ni ions in the nanocomposite films can be qualitatively understood from the large Pauling electronegativity of Ni (1.91) compared with that of Mn (1.55).

IV. CONCLUSION

In summary, we have designed and fabricated $(1 - x)$LMO : xNiO nanocomposite thin films. Detailed structure analysis substantiates that the 0D nanosized NiO particles are embedded into the 3D LMO matrix. Coexistence of robust FMI and EB properties is attributed to localized oxygen vacancy, preserved strain state, and ferromagnetic-antiferromagnetic interfacial interaction, which can prevent long-distance migration to enhance both resistivity and EB. The coexistence of FMIs and EB at low temperature has application potential for quantum and topological (magnonic) devices. This paper provides a referential strategy for developing materials with integrated functionalities and advantages for novel spintronic and spin-optical devices.

[1] Y. Kajiwara, K. Harii, S. Takahashi, J. Ohe, K. Uchida, M. Mizuguchi, H. Umezawa, H. Kawai, K. Ando, K. Takanashi, S. Maekawa, and E. Saitoh, Transmission of electrical signals by spin-wave interconversion in a magnetic insulator, Nature (London) **464**, 262 (2010).

[2] W. Lin, K. Chen, S. Zhang, and C. L. Chien, Enhancement of Thermally Injected Spin Current through an Antiferromagnetic Insulator, Phys. Rev. Lett. **116**, 186601 (2016).

[3] C. Du, T. van der Sar, T. X. Zhou, P. Upadhyaya, F. Casola, H. Zhang, M. C. Onbasli, C. A. Ross, R. L. Walsworth, Y. Tserkovnyak, and A. Yacoby, Control and local measurement of the spin chemical potential in a magnetic insulator, Science **357**, 195 (2017).

[4] A. Stupakiewicz, K. Szerenos, D. Afanasiev, A. Kirilyuk, and A. V. Kimel, Ultrafast nonthermal photo-magnetic recording in a transparent medium, Nature (London) **542**, 71 (2017).

[5] A. S. Erickson, S. Misra, G. J. Miller, R. R. Gupta, Z. Schlesinger, W. A. Harrison, J. M. Kim, and I. R. Fisher, Ferromagnetism in the Mott Insulator Ba_2NaOsO_6, Phys. Rev. Lett. **99**, 016404 (2007).

[6] D. C. Meng, H. J. Guo, Z. Z. Cuo, C. Ma, J. Zhao, J. B. Lu, H. Xu, Z. C. Wang, X. Hu, Z. P. Fu, R. R. Peng, J. H. Guo, X. F. Zhai, G. J. Brown, R. Knize, and Y. L. Lu, Strain-induced high-temperature perovskite ferromagnetic insulator, Proc. Natl. Acad. Sci. USA **115**, 2873 (2018).

[7] C. Sohn, E. Skoropata, Y. Choi, X. Gao, A. Rastogi, A. Huon, M. A. McGuire, L. Nuckols, Y. Zhang, J. W. Freeland, D. Haskel, and H. N. Lee, Room-temperature ferromagnetic insulating state in cation-ordered double-perovskite $Sr_2Fe_{1+x}Re_{1-x}O_6$ films, Adv. Mater. **31**, 1805389 (2019).

[8] S. Chakraverty, T. Matsuda, N. Ogawa, H. Wadati, E. Ikenaga, M. Kawasaki, Y. Tokura, and H. Y. Hwang, $BaFeO_3$ cubic single crystalline thin film: A ferromagnetic insulator, Appl. Phys. Lett. **103**, 142416 (2013).

[9] X. R. Wang, C. J. Li, W. M. Lü, T. R. Paudel, D. P. Leusink, M. Hoek, N. Poccia, A. Vailionis, T. Venkatesan, J. M. D. Coey, E. Y. Tsymbal, Ariando, and H. Hilgenkamp, Imaging and control of ferromagnetism in $LaMnO_3/SrTiO_3$ heterostructures, Science **349**, 716 (2015).

[10] Z. Chen, Z. Chen, Z. Q. Liu, M. E. Holtz, C. J. Li, X. R. Wang, W. M. Lü, M. Motapothula, L. S. Fan, J. A. Turcaud, L. R. Dedon, C. Frederick, R. J. Xu, R. Gao, A. T. N'Diaye, E. Arenholz, J. A. Mundy, T. Venkatesan, D. A. Muller, L.-W. Wang, J. Liu, and L. W. Martin, Electron Accumulation and Emergent Magnetism in $LaMnO_3/SrTiO_3$ Heterostructures, Phys. Rev. Lett. **119**, 156801 (2017).

[11] N. Biškup, J. Salafranca, V. Mehta, M. P. Oxley, Y. Suzuki, S. J. Pennycook, S. T. Pantelides, and M. Varela, Insulating Ferromagnetic LaCoO Films: A Phase Induced by Ordering of Oxygen Vacancies, Phys. Rev. Lett. **112**, 087202 (2014).

[12] T. Tsuyama, S. Chakraverty, S. Macke, N. Pontius, C. Schübler-Langeheine, H. Y. Hwang, Y. Tokura, and H. Wadati, Photoinduced Demagnetization and Insulator-to-Metal Transition in Ferromagnetic Insulating $BaFeO_3$ Thin Films, Phys. Rev. Lett. **116**, 256402 (2016).

[13] R. Q. Zhao, K. J. Jin, Z. T. Xu, H. Z. Guo, L. Wang, C. Ge, H. B. Lu, and G. Z. Yang, The oxygen vacancy effect on the magnetic property of the $LaMnO_{3-\delta}$ thin films, Appl. Phys. Lett. **102**, 122402 (2013).

[14] J. J. Peng, C. Song, B. Cui, F. Li, H. J. Mao, Y. Y. Wang, G. Y. Wang, and F. Pan, Exchange bias in a single $LaMnO_3$ film induced by vertical electronic phase separation, Phys. Rev. B **89**, 165129 (2014).

[15] L. M. Zheng, X. R. Wang, W. M. Lü, C. J. Li, T. R. Paudel, Z. Q. Liu, Z. Huang, S. W. Zeng, K. Han, Z. H. Chen, X. P. Qiu, M. S. Li, S. Yang, B. Yang, M. F. Chisholm, L. W. Martin, S. J. Pennycook, E. Y. Tsymbal, J. M. D. Coey, and W. W. Cao, Ambipolar ferromagnetism by electrostatic doping of a manganite, Nat. Commun. **9**, 1897 (2018).

[16] M. An, Y. K. Weng, H. M. Zhang, J. J. Zhang, Y. Zhang, and S. Dong, Appearance and disappearance of ferromagnetism in ultrathin $LaMnO_3$ on $SrTiO_3$ substrate: A viewpoint from first principles, Phys. Rev. B **96**, 235112 (2017).

[17] J. H. Lee, K. T. Delaney, E. Bousquet, N. A. Spaldin, and K. M. Rabe, Strong coupling of Jahn-Teller distortion to oxygen-octahedron rotation and functional properties in epitaxially strained orthorhombic $LaMnO_3$, Phys. Rev. B **88**, 174426 (2013).

[18] W. Zhang, L. Li, P. Lu, M. Fan, Q. Su, F. Khatkhatay, A. Chen, Q. Jia, X. Zhang, J. L. MacManus-Driscoll, and H. Wang, Perpendicular exchange-biased magnetotransport at the vertical heterointerfaces in $La_{0.7}Sr_{0.3}MnO_3$:NiO nanocomposites, ACS Appl. Mater. Interfaces **7**, 21646 (2015).

[19] J. Nogués, J. Sort, V. Langlais, V. Skumryev, S. Suriñach, J. S. Muñoz, and M. D. Baró, Exchange bias in nanostructures, Phys. Rep. **422**, 65 (2005).

[20] B. Dieny, V. S. Speriosu, S. S. P. Parkin, B. A. Gurney, D. R. Wilhoit, and D. Mauri, Giant magnetoresistance in soft ferromagnetic multilayers, Phys. Rev. B **43**, 1297(R) (1991).

[21] W. Zhang and K. M. Krishnan, Epitaxial exchange-bias systems: From fundamentals to future spin-orbitronics, Mater. Sci. Eng. R **105**, 1 (2016).

[22] M. Gibert, P. Zubko, R. Scherwitzl, J. Iniguez, and J.-M. Triscone, Exchange bias in $LaNiO_3$-$LaMnO_3$ superlattices, Nat. Mater. **11**, 195 (2012).

[23] X. K. Ning, Z. J. Wang, X. G. Zhao, C. W. Shih, and Z. D. Zhang, Exchange bias in $La_{0.7}Sr_{0.3}MnO_3$/NiO and $LaMnO_3$/NiO interfaces, J. Appl. Phys. **113**, 223903 (2013).

[24] M. Gibert, M. Viret, P. Zubko, N. Jaouen, J.-M. Tonnerre, A. Torres-Pardo, S. Catalano, A. Gloter, O. Stéphan, and J.-M. Triscone, Interlayer coupling through a dimensionality-induced magnetic state, Nat. Commun. **7**, 11227 (2016).

[25] H. M. Wei, J. L. Barzola-Quiquia, C. Yang, C. Patzig, T. Höche, P. Esquinazi, M. Grundmann, and M. Lorenz, Charge transfer-induced magnetic exchange bias and electron localization in

[26] A. K. Nayak, M. Nicklas, S. Chadov, P. Khuntia, C. Shekhar, A. Kalache, M. Baenitz, Y. Skourski, V. K. Guduru, A. Puri, U. Zeitler, J. M. D. Coey, and C. Felser, Design of compensated ferrimagnetic Heusler alloys for giant tunable exchange bias, Nat. Mater. **14**, 679 (2015).

[27] A. Migliorini, B. Kuerbanjiang, T. Huminiuc, D. Kepaptsoglou, M. Muñoz, J. L. F. Cuñado, J. Camarero, C. Aroca, G. Vallejo-Fernández, V. K. Lazarov, and J. L. Prieto, Spontaneous exchange bias formation driven by a structural phase transition in the antiferromagnetic material, Nat. Mater. **17**, 28 (2018).

[28] L. Y. Gao and A. A. Demkov, Spin-polarized two-dimensional t_{2g} electron gas: *Ab initio* study of EuO interface with oxygen-deficient $SrTiO_3$, Phys. Rev. B **97**, 125305 (2018).

[29] F. Gunkel, R. Waser, A. H. H. Ramadan, R. A. De Souza, S. Hoffmann-Eifert, and R. Dittmann, Space charges and defect concentration profiles at complex oxide interfaces, Phys. Rev. B **93**, 245431 (2016).

[30] R. Scherwitzl, S. Gariglio, M. Gabay, P. Zukbko, M. Gibert, and J.-M. Triscone, Metal-Insulator Transition in Ultrathin $LaNiO_3$ Films, Phys. Rev. Lett. **106**, 246403 (2011).

[31] G. N. Li, X. K. Huang, J. S. Hu, G. Song, and W. Y. Zhang, Strain relaxation induced coexistence of ferromagnetism and antiferromagnetism in (110)-oriented $LuMnO_3$ thin films on $YAlO_3$: A first-principles study, Phys. Rev. B **97**, 085140 (2018).

[32] X. Q. Yu, L. J. Wu, B. M. Zhang, H. Zhou, Y. Q. Dong, X. H. Wu, R. H. Kou, P. Yang, J. S. Chen, C. J. Sun, Y. M. Zhu, and G. M. Chow. Thickness-dependent polarization-induced intrinsic magnetoelectric effects in $La_{0.67}Sr_{0.33}MnO_3$/$PbZr_{0.52}Ti_{0.48}O_3$ heterostructures, Phys. Rev. B **100**, 104405 (2019).

[33] Z. D. Xu, S. B. Hu, R. Wu, J. O. Wang, T. Wu, and L. Chen, Strain-enhanced charge transfer and magnetism at a manganite/nickelate interface, ACS Appl. Mater. Interfaces **10**, 30803 (2018).

[34] L. X. Zhang, J. Chen, L. L. Fan, O. Diéguez, J. L. Cao, Z. Pan, Y. L. Wang, J. G. Wang, M. Kim, S. Q. Deng, J. O. Wang, H. H. Wang, J. X. Deng, R. B. Yu, J. F. Scott, and X. R. Xing, Giant polarization in super-tetragonal thin films through interphase strain, Science **361**, 494 (2018).

[35] X. Sun, J. Huang, J. Jian, M. Fan, H. Wang, Q. Li, J. L. MacManus-Driscoll, P. Lu, X. Zhang, and H. Wang, Three-dimensional strain engineering in epitaxial vertically aligned nanocomposite thin films with tunable magnetotransport properties, Mater. Horiz. **5**, 536 (2018).

[36] E.-M. Choi, A. D. Bernardo, B. Zhu, P. Lu, H. Alpern, K. H. L. Zhang, T. Shapira, J. Feighan, X. Sun, J. Robinson, Y. Paltiel, O. Millo, H. Wang, Q. Jian, and J. L. MacManus-Driscoll, 3D strain-induced superconductivity in $La_2CuO_{4+\delta}$ using a simple vertically aligned nanocomposite approach, Sci. Adv. **5**, eaav5532 (2019).

[37] See Supplemental Material at http://link.aps.org/supplemental/10.1103/PhysRevB.101.014422 for the XRD patterns of LMO:NiO ceramic targets and films, RSMs of the LMO/STO heterostructure, in-plane and out-of-plane *M-H* loops of LMO:NiO films and corresponding H_{EB} values, and out-of-plane *M-H* loops of the NiO/STO heterostructure.

(111)- and (001)-oriented $LaNiO_3$/$LaMnO_3$ superlattices, Appl. Phys. Lett. **110**, 102403 (2017).

[38] S. Chandra, A. I. Figueroa, B. Garnali, M. H. Phan, H. Srikanth, and A. K. Raychaudhuri, Phase coexistence and magnetic anisotropy in polycrystalline and nanocrystalline $LaMnO_{3+\delta}$, J. Appl. Phys. **109**, 07D720 (2011).

[39] M. Snamina and A. M. Oleś, Spin-orbital model of stoichiometric $LaMnO_3$ with tetragonal distortions, Phys. Rev. B **97**, 104417 (2018).

[40] P. E. Tomaszewski, N. Miniajluk, M. Zawadzki, and J. Trawczyński, X-ray study of structural phase transitions in nanocrystalline $LaMnO_{3+\delta}$ perovskite, Phase Transitions **92**, 525 (2019).

[41] Z. L. Zhang, W. Sigle, and W. Kurtz, HRTEM and EELS study of screw dislocation cores in $SrTiO_3$, Phys. Rev. B **69**, 144103 (2004).

[42] I. Sugiyama, N. Shibata, Z. Wang, S. Kobayashi, T. Yamamoto, and Y. Ikuhara, Ferromagnetic dislocations in antiferromagnetic NiO, Nat. Nanotechnol. **8**, 266 (2013).

[43] X. L. Wang, P. S. Ku, Q. Shao, W. F. Cheng, C. W. Leung, and A. Ruotolo, Magnetism as a probe of the origin of memristive switching in p-type antiferromagnetic NiO, Appl. Phys. Lett. **103**, 223508 (2013).

[44] I. Marozau, P. T. Das, M. Döbeli, J. G. Storey, M. A. Uribe-Laverde, S. Das, C. N. Wang, M. Rössle, and C. Bernhard, Influence of La and Mn vacancies on the electronic and magnetic properties of $LaMnO_3$ thin films grown by pulsed laser deposition, Phys. Rev. B **89**, 174422 (2014).

[45] R. H. Kodama, S. A. Makhlouf, and A. E. Berkowitz, Finite Size Effects in Antiferromagnetic NiO Nanoparticles, Phys. Rev. Lett. **79**, 1393 (1997).

[46] J. M. Vila-Fungueiriño, B. Rivas-Murias, B. Rodríguez-González, O. Txoperena, D. Ciudad, L. E. Hueso M. Lazzari, and F. Rivadulla, Room-temperature ferromagnetism in thin films of $LaMnO_3$ deposited by a chemical method over large areas, ACS Appl. Mater. Interfaces **7**, 5410 (2015).

[47] S. Huang, K. Ruan, Z. Lv, L. Zhuang, P. Wei, H. Wu, M. Li, J. Zhang, Y. Chai, H. Yang, L. Cao, and X. Li, Magnetic and transport properties in layered $Nd_{1-x}Sr_{1+x}CoO_4$, Phys. Rev. B **73**, 094431 (2006).

[48] C. Piamonteze, M. Gibert, J. Heidler, J. Dreiser, S. Rusponi, H. Brune, J.-M. Triscone, F. Nolting, and U. Staub, Interfacial properties of $LaMnO_3/LaNiO_3$ superlattices grown along (001) and (111) orientations, Phys. Rev. B **92**, 014426 (2015).

[49] M. Abbate, F. M. F. de Groot, J. C. Fuggle, A. Fujimori, O. Strebel, F. Lopez, M. Domke, G. Kaindl, G. A. Sawatzky, M. Takano, Y. Takeda, H. Eisaki, and S. Uchida, Controlled-valence properties of $La_{1-x}Sr_xFeO_3$ and $La_{1-x}Sr_xMnO_3$ studied by soft-x-ray absorption spectroscopy, Phys. Rev. B **46**, 4511 (1992).